Published in final edited form as:
Nat Mater. 2015 August ; 14(8): 820–825. doi:10.1038/nmat4352.

Synthesis of nanostructures in nanowires using sequential catalyst reactions

F. Panciera[1,2], **Y.-C. Chou**[2,3,4], **M.C. Reuter**[2], **D. Zakharov**[4], **E.A. Stach**[4], **S. Hofmann**[1,*], and **F.M. Ross**[2,*]

[1]Department of Engineering, University of Cambridge, 9 J. J. Thomson Avenue, Cambridge CB3 0FA, UK

[2]IBM Research Division, T. J. Watson Research Center, Yorktown Heights, NY 10598, USA

[3]Department of Electrophysics, National Chiao Tung University, 1001 University Road, Hsinchu city, Taiwan

[4]Center for Functional Nanomaterials, Brookhaven National Laboratory, Upton, NY 11973, USA

Abstract

Nanowire growth by the vapor-liquid-solid process enables a high level of control over nanowire composition, diameter, growth direction, branching and kinking, periodic twinning, and crystal structure. The tremendous impact of VLS-grown nanowires is due to this structural versatility, generating applications ranging from solid state lighting and single photon sources to thermoelectric devices. Here we show that the morphology of these nanostructures can be further tailored by using the liquid droplets that catalyze nanowire growth as a “mixing bowl”, in which growth materials are sequentially supplied to nucleate new phases. Growing within the liquid, these phases adopt the shape of faceted nanocrystals that are then incorporated into the nanowires by further growth. We demonstrate this concept by epitaxially incorporating metal silicide nanocrystals into Si nanowires with defect-free interfaces, and discuss how this process can be generalized to create complex nanowire-based heterostructures.

The ability to control the fabrication of materials at sub-100 nm dimensions is crucial to tailoring properties and functionalities. The technologies opened up are highlighted by the evolution of electronic and photonic devices over the last decades. Bottom-up, or self-assembly, approaches to nanofabrication are particularly important because of the demands for increasing diversity of materials, greater structural complexity, and strict requirements for control of the interfaces between the component materials. In this context, the vapor-liquid-solid (VLS) growth mechanism [1,2,3,4,5,6] has been extensively explored. VLS growth is versatile, enabling a high level of control over nanowire composition to form axial and radial nanowire heterostructures, as well as control over nanowire diameter, growth

*Corresponding authors fmross@us.ibm.com, sh315@cam.ac.uk.

Author contributions: FP and YCC performed experiments and data analysis, MCR developed the UHV TEM technique, DZ and EAS performed high resolution ETEM experiments, and SH and FMR designed the experiments and coordinated the analysis.

Europe PMC Funders Author Manuscripts

direction and kinking, branching, periodic twinning, and crystal structure [7,8,9,10,11,12,13,14,15]. Each type of nanowire morphology suggests further applications, such as heterostructures with precisely defined surface facets for solid state lighting [16,17]; crystal phase quantum dots, proposed for single photon sources [18], and periodically twinned nanowires for thermoelectric devices [19]. Here, we report an expansion of the catalytic VLS growth concept which opens an additional pathway to tailor complex nano-heterostructures. We supply growth materials sequentially to the liquid droplets that catalyze nanowire growth to nucleate new phases that form as nanocrystals and can be incorporated into the nanowires with epitaxially perfect interfaces. We use *in situ* transmission electron microscopy (TEM) to directly record each step of this "sequential catalyst reaction" process. We illustrate the concept by forming metal silicide endotaxial nano-inclusions in Si nanowires, and assess its generality and flexibility for creating more complex nanostructured nanowires.

Figure 1 shows an overview of the process by which $NiSi_2$ nanocrystals can be formed and incorporated into Si nanowires. We carry out the reaction sequence in an ultrahigh vacuum transmission electron microscope (UHVTEM) [20] to provide a controlled growth environment (see Methods). Si (111) nanowires, 20-50 nm in radius and 100-150nm in length, are synthesized using Au as the catalytic metal and disilane (Si_2H_6) as the precursor gas. After cooling (still under UHV), ~1 nm Ni is deposited by evaporation. The sample is then annealed *in situ* for 30 min at 200°C in an O_2 pressure of 1×10^{-5} Torr. This oxidation step forms a layer of SiO_2 on the nanowire sidewalls [21] (Supplementary Information, Figure S1), enabling selective introduction of Ni into the catalyst without sidewall reactions. A similar outcome will be described below that makes use of a metal-organic precursor such as nickelocene that incorporates Ni selectively into the droplet without requiring oxidation.

After this oxidation step, the temperature is set to 350°C, a value just below the Au-Si eutectic temperature, and 1×10^{-5} Torr Si_2H_6 is introduced (Fig. 1a). The nanowires are slowly heated to 500°C at ~10°C/min. As the temperature passes the eutectic point, the liquid AuSi droplet reforms (Fig. 1b) as the solid Au abruptly reacts with Si in the nanowire. Simultaneously Ni and Si react. These reactions consume part of the nanowire (Fig. 1b). The outcome of the Ni-Si reaction is surprising. Inside the droplet, bright contrast appears instantaneously as the catalyst becomes liquid, revealing the presence of a solid inclusion. This solid may be a single octahedral nanocrystal, or smaller nanocrystals (as in Fig. 1b) that coalesce into a single octahedral $NiSi_2$ nanocrystal as the temperature continues to increase (Fig. 1c). Note that the $NiSi_2$ phase forms in the liquid rather than at the nanowire growth front. Once formed, its volume remains constant but it moves randomly within the liquid droplet (Supplementary Information, Movie 1). Eventually, it "docks" onto the nanowire (Fig. 1d), touching the nanowire growth interface and forming a defect-free, epitaxial connection (Fig. 1i and j); note the excellent registry (~0.4% mismatch) between Si and $NiSi_2$ lattices. During this time, the nanowire continues to grow. Growth is slow due to the low temperature, but initially planarizes the nanowire-catalyst interface. As the temperature is raised, the growth rate increases (~2.5 nm/min at 500°C [22]), and the docked nanocrystal is incorporated into the Si matrix (Fig. 1e-h). The result is a nanowire containing an inclusion. We confirm the $NiSi_2$ phase from the lattice parameter, shape (typical of a cubic

phase) and volume (see below), and show that perfect endotaxial incorporation is possible (Fig. 1k-m).

The entire sequential catalyst reaction process, from the deposition of Ni to the growth of the nanowire, can be repeated and multiple silicides can be embedded to form a complex silicide/silicon heterostructure (Supplementary Information, Figure S2). The distance between nanocrystals inside the wire is controlled through the growth time between Ni deposition steps, and the size of each nanocrystal is controlled by the amount of deposited Ni. Starting with free-standing nanowires is important in this reaction sequence. For nanowires dispersed on a silicon nitride membrane, $NiSi_2$ has been observed to nucleate in the AuSi droplet [23], but the nanocrystal does not move or dock to the nanowire, presumably because the membrane acts as a preferential nucleation site.

How it is possible to have such good epitaxy between Si and the $NiSi_2$ nanocrystal, given that the nanocrystal forms in the liquid phase and appears to touch and “dock” to the Si surface in one step? Images such as those in Fig. 1 and Movie 1 cannot resolve the atomic level details of the docking process. In Fig. 2 and Movie 2, we therefore show the process as observed in an aberration corrected environmental TEM (ETEM) equipped with gas handling capabilities for Si_2H_6 [24] and a fast camera (see Methods). The sequence shown in Fig. 2 was observed in several instances. First, the octahedral particle makes contact with the Si (111) growth interface by touching at a single edge; second, it completes the epitaxial connection via rotation around the [110] axis (Fig. 2a). The angle between the silicide nanocrystal and Si is readily measured (Fig. 2b) through FFT of the image series. Rotation takes place in a stepwise manner and a single increment can occur in less than 0.1 second (Fig. 2c). The driving force of this two-step mechanism presumably is based on minimization of interface energies of the two crystals. By analogy to what has been observed for axiotaxial structures [25], even when only one family of planes is aligned, there is an energy gain sufficient to align the nanocrystal with the nanowire (the initial edge contact). The subsequent stepwise rotation can be understood by noting that the nanocrystal shape appears unchanged during rotation, but the Si surface shows steps that flow readily during rotation. The Si rearranges to accommodate the silicide, apparently by moving atoms from the right side to the left: Si layers on the right of the silicide retract and a new layer appears on the left (Fig. 2d). At each rotation increment, a step moves (Movie 2) increasing the contact area forming the low energy epitaxial connection. During subsequent nanowire growth that fully incorporates nanocrystals, we observe rapid step flow (Movie 3), similar to that observed in conventional nanowire growth [26,27]. We suggest that the highly mobile nature of the Si surface during docking and subsequent nanowire growth enables the production of highly perfect crystal structures in which silicides can be endotaxially incorporated without any evidence of dislocations.

The docking process does not always result in perfect endotaxy. Occasionally nanocrystals make contact with the Si surface in an apparently unfavourable orientation and do not reorient before the nanowire starts to grow. An example is shown in Movie 4 (Supplementary Information), where Si grows around a misoriented nanocrystal. The Si growth front remains planar. Defects are visible at the silicide/Si interface but the surrounding Si appears defect-free. This suggests that each Si ledge nucleates at the

periphery of the growth front (as in conventional VLS, [26]) rather than at the interior junction surrounding the silicide, and hints that it could be generally possible to grow high quality Si by VLS around inclusions, even if they are not well matched to or aligned with the Si lattice.

A key feature of the sequential catalyst reaction concept is the formation of a single, faceted nanocrystal which later attaches to its nanowire. We presume that the liquid-mediated reaction helps to allow easy coalescence if multiple nuclei form initially, and easy rearrangement of the new phase into a well-defined, low energy shape. But why does the nanocrystal form in the liquid (or at its surface), rather than at the Si interface, especially in this case, where there is an excellent lattice match between $NiSi_2$ and Si? Experiments such as that in Fig. 1 cannot address this question: $NiSi_2$ forms too quickly to resolve as the temperature is raised, since Si is present in excess (from the nanowire). We therefore designed experiments where Si is added more gradually to metal particles, slowing down the reaction sequence so that we can understand the Au-Ni-Si system better by examining the phases and nucleation sites in more detail.

In Fig. 3, Au and Ni were deposited sequentially on an electron transparent, inert membrane and annealed in vacuum to agglomerate into crystallites (see Methods). Then the temperature was fixed and Si_2H_6 was supplied. Figs. 3a, b and Movie 5 show the resulting sequence of phases observed respectively in the ETEM (Fig. 3a and Movie 5) and UHV-TEM (Fig. 3b). This fairly complex sequence can be understood by comparison with the reaction of pure Au with Si under similar conditions [28,29]. In that case, the initial reaction of Si with an Au crystallite forms liquid AuSi at the Au surface. The reaction front then propagates inwards [28]. Once all the Au is consumed, but Si is still being supplied, the AuSi eutectic becomes supersaturated with Si. Eventually solid Si nucleates at the periphery of the droplet [29,30].

In Figures 3a and 3b, however, a new phase forms before any substantial reaction of Au with Si. (A thin liquid layer would not be visible.) It is clear from the size of this phase (Fig. 3c) that its volume is fixed by the initial amount of Ni. We assume therefore that it is a Ni-silicide. Only after its growth is complete does the solid Au react with Si to form AuSi. The initial Ni-silicide is elliptical in projection. However, once the Au is consumed, and presumably Si starts to supersaturate the liquid, the silicide increases in volume (Fig. 3c) by a factor of ~2 and becomes a well-faceted octahedron. This final phase is unequivocally $NiSi_2$; the initial phase is presumably a Ni-rich silicide, which we cannot identify unambiguously because of the large number of Ni-rich silicides in the Ni-Si phase diagram (Table S1 in Supplementary Information). Eventually, solid Si nucleates and grows at the periphery of the droplet. And crucially, the $NiSi_2$ and Si come into contact only at the end of the sequence.

The timing of the transition from Ni-rich silicide to $NiSi_2$ appears to depend on the conditions used: the data in Figs. 3b and 3c is consistent with a transition occurring after all Au has reacted to form AuSi, while in Fig. 3a the characteristic $NiSi_2$ facetted shape is visible earlier, even when crystalline Au is still present. However, in all cases, the phase that makes the epitaxial connection to Si is $NiSi_2$. The size of this phase can be accurately

controlled by adjusting the amount of Ni deposited (Fig. 3d and 3e) and the smallest we have realized is < 3 nm in radius (Fig. 3a).

Overall, the data in Fig. 3 shows that a silicide forms before Si reacts with Au. The fact that the reactions in Fig. 1 take place at a nanowire tip rather than in an isolated Au particle, as in Fig. 3, therefore does not play a role in the overall process. Indeed, if we hold nanowires below the eutectic temperature, so that AuSi liquid can not form quickly, we observe silicides nucleating while the Au at the nanowire tip remains solid (Fig. S3). If an initial silicide forms and attaches only after it has transformed to $NiSi_2$, then the final quality of the silicide/Si epitaxy is determined exclusively by the liquid-mediated contact process described in Fig. 2.

We finally consider the yield, uniformity and generality of the sequential catalyst reaction concept, central in developing applications of this nanostructured material. Yield and uniformity in *in situ* experiments are expected to be poor, because of the small growth area, uncontrolled catalyst sizes and shadowing during the shallow angle Ni evaporation. Even so, nanowires of median size (r~40 nm) reliably produce nanocrystals in over 90% of droplets. However, yield loss occurs because all but 5% of wires kink during the incorporation step. This is unsurprising because cooling Si nanowires, as required here for transfer to the evaporator, is known to cause kinking on regrowth [7]. We have solved this issue by using a gaseous metal MOCVD precursor, nickelocene (bis(cyclopentadienyl)Ni, $Ni(C_5H_5)_2$), to selectively deposit Ni into the droplets without the need for cooling. This avoids kinking, also eliminates the need for the sidewall oxidation step (see below), and is promising for its compatibility with large scale production; its main issue is carbon contamination. We therefore believe that yield and uniformity can be addressed through an optimized gaseous precursor such as Ni carbonyl or an *in situ* metal evaporator, in concert with size-controlled catalysts.

To address the generality of the process, we have investigated several other materials systems. We have nucleated single, well-faceted nanocrystals by supplying Co and Mn to liquid AuSi catalysts (Figs 4a and b, respectively) analogous to the process for Ni. In Fig. 4a, the $CoSi_2$ nanocrystal was formed using cobaltocene, i.e. bis(cyclopentadienyl)Co, or $Co(C_5H_5)_2$. The sidewalls were not passivated by oxidation, yet showed no visible silicide formation. In Fig. 4b, Mn monosilicide was formed using evaporated Mn; manganocene produces similar results (not shown). For Mn, an epitaxial connection forms (Fig. 4c) but does not lead to incorporation because the nanocrystal detaches as Si ledges start to flow when Si growth is restarted. We suppose that the interface is not particularly low energy due to the mismatch, and speculate that for smaller crystals with lower total strain energy it may be possible to complete the incorporation. Finally, Fig. 4d shows a NiGa nanocrystal formed via nickelocene exposure of an AuGa droplet at the tip of a GaAs nanowire.

Although the limited number of systems we have explored does not allow us to infer a model that predicts whether a given materials combination will produce endotaxial nanocrystals, we can provide some necessary conditions (Supplementary Information, Fig. S4). The first is the formation of a compact nanocrystal instead of a full layer of the new material. It has already been shown [31] that this requires a specific relationship between the interface

energies of the various crystals. Endotaxy implies additional constraints: the new crystal should be completely wetted by the liquid catalyst, and there must be a driving force for attachment, as discussed in the Supporting Information. This simple thermodynamic argument can perhaps guide materials choice, especially in cases where the relevant energies can be estimated.

In conclusion, we have introduced a technique that extends the VLS method of nanowire growth, allowing the formation of nanowires that contain embedded nanocrystals. In essence, the catalyst particle is used not only to grow nanowires, as in the classic VLS process, but in an extended role, to independently nucleate different nanocrystals, whose formation and attachment in the liquid contribute to the high nanocrystal/nanowire interface quality. Using *in situ* TEM, we have explored this process in detail for Ni, embedding $NiSi_2$ quantum dots within Si nanowires with defect-free interfaces, and with a size and relative position controlled by the amount of Ni supplied and by the growth time between nucleation events. *In situ* microscopy reveals the process by which the epitaxial interface is created, and factors that influence nanocrystal location and phase. We have described how this sequential catalyst reaction concept can apply to other metals and nanowire materials, and introduced different pathways to selectively supply the metal. In particular for metalorganic precursors, the catalytic droplet can be thought of as a “mixing bowl” where the order and amount of each ingredient can be programmed to make a desired recipe with the aim of achieving controlled growth of complex nanostructures containing quantum dots of precise dimensions in single nanowires. This method is complementary to the formation of fully embedded quantum dots by shell growth on axially modulated nanowires [32,33]. Such quantum dots are limited in diameter by the initial nanowire diameter, and only certain materials combinations produce good quantum dot morphologies [31]. Sequential catalyst reactions allow compact quantum dots to be formed with dimensions decoupled from the nanowire diameter, including in materials that do not grow by VLS but present technological interest. The embedded nanocrystals can be located at p-n junctions or compositional interfaces to enhance their functionality.

The materials system on which we have focused has central relevance for microelectronics applications since Ni silicides are the material of choice for contact fabrication in CMOS technology. Ni and Co silicides also have magnetic and plasmonic properties that make them appealing for a wide range of applications. One such application could be in photodetectors. The dielectric functions of silicides show metallic behavior in the infrared and visible ranges and the manufacturing advantages of silicides make them promising materials for infrared plasmonics integrated on microelectronic devices [34,35,36]. Si nanowire based photodetectors [37] are generally coupled with metallic waveguides or nanoparticles to improve their efficiency [38]. $NiSi_2$ [39] or $CoSi_2$ [40] nanoparticles embedded at the p-n junction of a photodetector would be expected to enhance light absorption by exciting localized surface plasmon resonances. The method described here can in principle provide the building blocks for such devices. Quantum transport provides another possible application. Nanoscale PtSi clusters in a Si nanowire offer a unique potential for realizing “Coulomb blockade” transistors and other single-electron devices [41]; such silicide quantum dots have been formed accidentally during fabrication of PtSi contacts to the nanowire, but we can now see how to form such structures in a controlled way. High-density

memories, semiconductor lasers, and tunnel diodes are other areas of interest. For integrated electronics, epitaxial metallization incorporated into vertically-grown semiconductor heterostructures opens up new possibilities by providing buried interconnects of atomic perfection, along with the capability to engineer a wide range of three-dimensional device structures. We therefore suggest that sequential catalyst reactions will open up exciting opportunities for the controlled growth and device integration of complex nanostructures with tailored functionalities.

Methods

Nanowire growth was performed in a Hitachi H-9000 UHV-TEM having a base pressure of 2×10^{-10} Torr and a maximum pressure during imaging of 2×10^{-5} Torr. The microscope is connected to a cluster of UHV tools where temperature calibration and metal deposition were carried out. The substrates used for nanowire growth were 3 mm × 300 μm silicon strips cut from a 700 μm thick (111) wafer, and were imaged with the polished (111) surface parallel to the beam. Each sample was cleaned chemically finishing with an HF dip and was then loaded into a sample holder cartridge that can heat the sample by passing a direct current through it. After introducing the sample into the UHV environment, the cartridge was degassed and any surface oxide was desorbed by heating above 1200°C. The temperature was measured with a pyrometer and an *ex situ* calibration of temperature vs. current was performed. 1-2 nm of Au was then deposited by electron beam evaporation and the sample was loaded in the microscope where precursor gas (Si_2H_6) was introduced through a capillary tube at a pressure of 2×10^{-5} Torr. The temperature was raised to 500°C in order to agglomerate Au into droplets and initiate VLS growth. Subsequently, Ni or other metal evaporation was performed in the same UHV tool using an electron beam evaporator. For each metal evaporation step, a crystal monitor was used to measure the thickness of the deposited metal. The crystal monitor reading was calibrated via using medium energy ion scattering measurement of samples with different thicknesses of deposited metal. Alternatively, Ni or other metals could be deposited by exposure to nickelocene or analogous reactive gas precursors, but without any calibration of the amount deposited.

High resolution imaging was carried out in a FEI Titan 300 aberration-corrected ETEM. Samples on which nanowires had been pre-grown and Ni had then been deposited in the UHV-TEM were carried through air, cleaned with an HF vapor etch, then loaded into the ETEM. A shell of SiO_2 remained visible around the nanowires but this could be removed by condensing the intense electron beam spot around the nanowire catalyst droplet while holding the sample at 500°C. Images were recorded using a Gatan K2 camera acquiring 400 images per second each having 4 mega-pixels.

Nucleation experiments were performed on 50 nm thick silicon nitride windows formed by etching the substrate away over a ~100 × 100 μm^2 region in the center of a 3 × 3 mm^2 sample that had been diced from a nitride-coated Si wafer. 1-2 nm of Au was evaporated onto such samples and agglomerated by heating, or alternatively, Au aerosol nanoparticles were deposited directly onto the samples. Ni or other metals were then added by evaporation or gas phase precursor, as described above. The membrane samples were heated by direct current with the temperature calibrated by pyrometer.

Supplementary Material

Refer to Web version on PubMed Central for supplementary material.

Acknowledgments

Supported by the National Science Foundation under Grants No. DMR-0606395 and 0907483 (YCC), ERC Grant 279342: InSituNANO (FP, SH), the National Science Council of Taiwan under Grant No. NSC-101-2112-M-009-021-MY3 (YCC), the Center for Interdisciplinary Science under the MOE-ATU project for NCTU (YCC) and the Center for Functional Nanomaterials, Brookhaven National Laboratory, which is supported by the U.S. Department of Energy, Office of Basic Energy Sciences, under contract DE-AC02-98CH10886 (DZ and EAS). The authors acknowledge Andrew Gamalski for assistance with high resolution imaging, Cory Czarnik for assistance with image processing and Arthur Ellis for technical support.

References

1. Wagner RS, Ellis WC. Vapor-liquid-solid mechanism of single crystal growth. Appl Phys Lett. 1964; 4:89–91.
2. Hiruma K, et al. Growth and optical properties of nanometer-scale GaAs and InAs whiskers. J Appl Phys. 1995; 77:447.
3. Lauhon LJ, Gudiksen MS, Wang D, Lieber CM. Epitaxial core–shell and core–multishell nanowire heterostructures. Nature. 2002; 420:57–61. [PubMed: 12422212]
4. Samuelson L. Self-forming nanoscale devices. Mater Today. 2003; 10:22–31.
5. Law M, Goldberger J, Yang P. Semiconductor nanowires and nanotubes. Annu Rev Mater Sci. 2004; 34:83–122.
6. Schwalbach EJ, Voorhees PW. Phase equilibrium and nucleation in VLS-grown nanowires. Nano Lett. 2008; 8(11):3739–3745. [PubMed: 18954122]
7. Tian B, Xie P, Kempa TJ, Bell DC, Lieber CM. Single-crystalline kinked semiconductor nanowire superstructures. Nature Nanotechnology. 2009; 4:824–829.
8. Adhikari H, Marshall AF, Chidsey CED, McIntyre PC. Germanium nanowire epitaxy: Shape and orientation control. Nano Lett. 2006; 6:319–323.
9. Dick KA, et al. Synthesis of branched ‘nanotrees’ by controlled seeding of multiple branching events. Nature Mater. 2004; 3:380–384. [PubMed: 15122221]
10. Burgess T, et al. Twinning superlattice formation in GaAs nanowires. ACS Nano. 2013; 7:8105–8114. [PubMed: 23987994]
11. Wen C-Y, et al. Formation of compositionally abrupt axial heterojunctions in silicon-germanium nanowires. Science. 2009; 326:1247–1250. [PubMed: 19965471]
12. Lehmann S, Jacobsson D, Deppert K, Dick KA. High crystal quality wurtzite-zinc blende heterostructures in metal-organic vapor phase epitaxy-grown GaAs nanowires. Nano Res. 2012; 5:470–476.
13. Caroff P, et al. Controlled polytypic and twin-plane superlattices in III–V nanowires. Nature Nanotech. 2009; 4:50–55.
14. Algra RE. Twinning superlattices in indium phosphide nanowires. Nature. 2008; 456:369–372. [PubMed: 19020617]
15. Joyce HJ, Wong-Leung J, Gao Q, Tan HH, Jagadish C. Phase perfection in zinc blende and wurtzite III–V nanowires using basic growth parameters. Nano Lett. 2010; 10:908–915. [PubMed: 20131909]
16. Huang MH, et al. Room-temperature ultraviolet nanowire nanolasers. Science. 2001; 292:1897. [PubMed: 11397941]
17. Duan X, Huang Y, Cui Y, Wang J, Lieber CM. Indium phosphide nanowires as building blocks for nanoscale electronic and optoelectronic devices. Nature. 2001; 409:66. [PubMed: 11343112]
18. Akopian N, Patriarche G, Liu L, Harmand J-C, Zwiller V. Crystal phase quantum dots. Nano Lett. 2010; 10:1198–1201. [PubMed: 20205446]

19. Hochbaum AI, et al. Enhanced thermoelectric performance of rough silicon nanowires. Nature. 2008; 451:163. [PubMed: 18185582]
20. Ross FM. Controlling nanowire structures through real time growth studies. Rep Prog Phys. 2010; 73:114501.
21. Bartur M, Nicolet MA. Thermal oxidation of nickel disilicide. Appl Phys Lett. 1982; 40:175.
22. Kallesøe C, Wen C-Y, Mølhave K, Bøggild P, Ross FM. Measurement of local Si-nanowire growth kinetics using in situ transmission electron microscopy of heated cantilevers. Small. 2010; 6:2058–2064. [PubMed: 20730823]
23. Tang W, et al. Gold catalyzed Nickel disilicide formation: A new Solid–Liquid–Solid phase growth mechanism. Nano Lett. 2013; 13:6009–6015. [PubMed: 24274698]
24. Chou Y-C, et al. 2015 in preparation.
25. Detavernier C, et al. An off-normal fibre-like texture in thin films on single-crystal substrates. Nature. 2003; 426:641–645. [PubMed: 14668858]
26. Wen C-Y, et al. Periodically changing morphology of the growth interface in Si, Ge, and GaP nanowires. Phys Rew Lett. 2011; 107:025503.
27. Gamalski AD, Ducati C, Hofmann S. Cyclic Supersaturation and triple phase boundary dynamics in germanium nanowire growth. J Phys Chem C. 2011; 115:4413–4417.
28. Kim BJ, et al. Determination of size effects during the phase transition of a nanoscale Au-Si eutectic. Phys Rev Lett. 2009; 103:155701. [PubMed: 19905650]
29. Kim BJ, et al. Kinetics of individual nucleation events observed in nanoscale Vapor-Liquid-Solid growth. Science. 2008; 322:1070. [PubMed: 19008438]
30. Hofmann S, et al. Ledge-flow-controlled catalyst interface dynamics during Si nanowire growth. Nature Mater. 2008; 7(5):372–375. [PubMed: 18327262]
31. Dick KA, et al. The morphology of axial and branched nanowire heterostructures. Nano Lett. 2007; 7:1817–1822. [PubMed: 17489640]
32. Wu Y, Fan R, Yang P. Block-by-block growth of single-crystalline Si/SiGe superlattice nanowires. Nano Lett. 2002; 2:83–86.
33. Gudiksen MS, Lauhon LJ, Wang J, Smith DC, Lieber CM. Growth of nanowire superlattice structures for nanoscale photonics and electronics. Nature. 2010; 415:617–620. [PubMed: 11832939]
34. Soref R, et al. Longwave plasmonics on doped silicon and silicides. Optics Express. 2008; 16:6507–6514. [PubMed: 18545354]
35. Naik GV, Vladimir MS, Alexandra B. Alternative plasmonic materials: beyond gold and silver. Advanced Materials. 2013; 25:3264–3294. [PubMed: 23674224]
36. Mooney JM, Silverman J. The theory of hot-electron photoemission in Schottky-barrier IR detectors. IEEE Trans Electron Devices. 1985; 32:33.
37. Fan P, et al. An invisible metal–semiconductor photodetector. Nature Photonics. 2012; 6:380–385.
38. Jee S-W, et al. A silicon nanowire photodetector using Au plasmonic nanoantennas. Nano Convergence. 2014; 1:1–7.
39. Shiyang Zhu HS, et al. Waveguide-integrated near-infrared detector with self-assembled metal silicide nanoparticles embedded in a silicon p-n junction. Appl Phys Lett. 2012; 100:061109.
40. Fathauer RW, et al. Infrared photodetectors with tailorable response due to resonant plasmon absorption in epitaxial silicide particles embedded in silicon. Appl Phys Lett. 1993; 62:1774.
41. Mongillo M, Spathis P, Katsaros G, De Franceschi S. PtSi clustering in silicon probed by transport spectroscopy. Phys Rev X. 2013; 3:041025.
42. Park, J-H.; Sudarshan, TS. Chemical vapor deposition. 1st ed. ASM International; Scarborough: 2001.

Europe PMC Funders Author Manuscripts

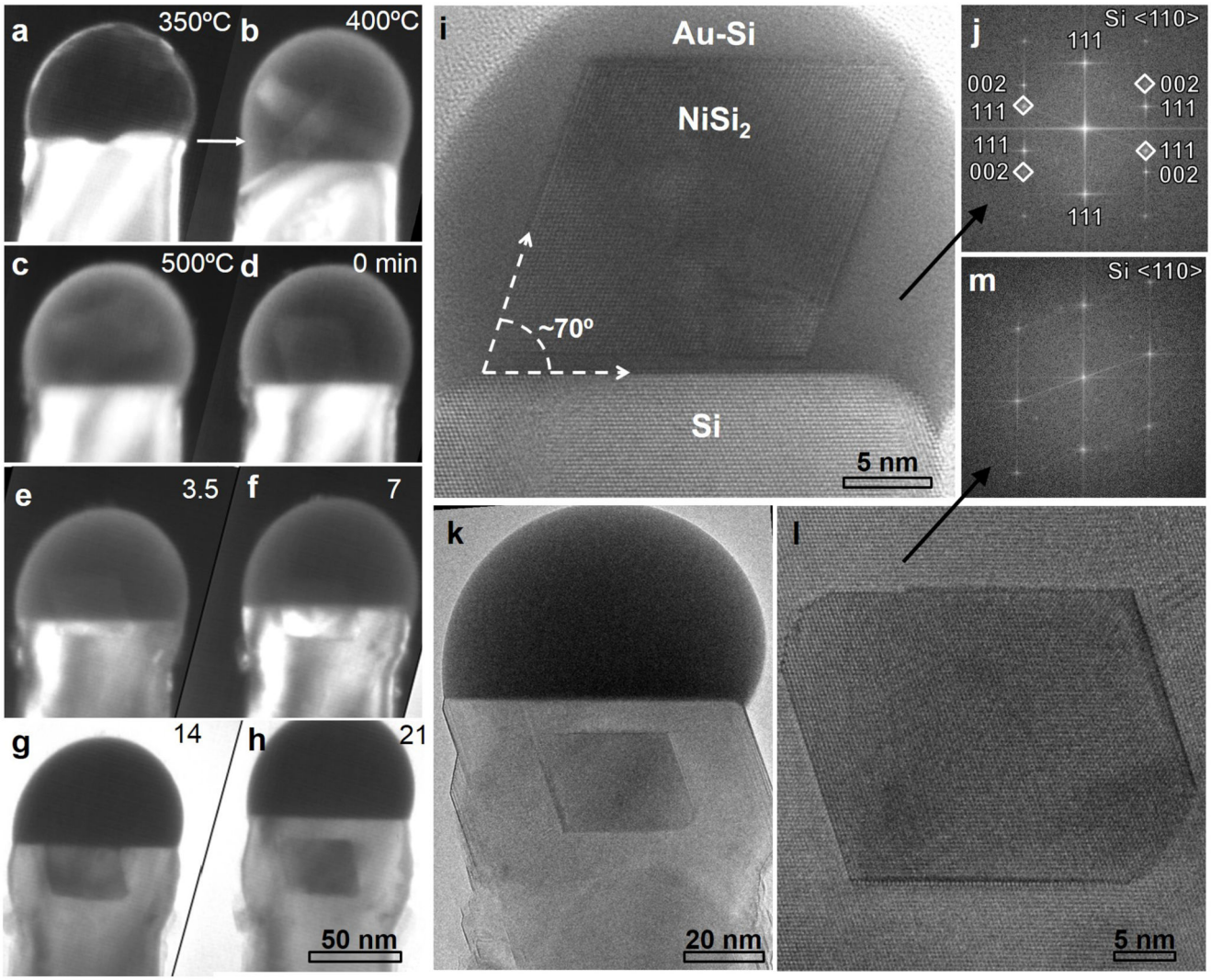

Figure 1.

TEM images showing nickel silicide formation and incorporation in Si nanowires. **a-d** Sequence of dark field (DF) images recorded after Ni deposition and oxidation, while raising the temperature to 500°C in 5×10^{-5} Torr Si_2H_6. A $NiSi_2$ nanocrystal forms inside the AuSi droplet and makes epitaxial contact with Si. The arrow in **b** shows the initial Au/Si interface. **e-h** Nanowire growth that embeds the nanocrystal as the temperature reaches 500°C. The growth rate is steady, apart from in the first few minutes where it is slowed, perhaps by impurities formed at the catalyst surface during oxidation. Bright field conditions are used in **g** and **h** to highlight the structure. The time is given in seconds. **i, j** High-resolution image and Fast Fourier transform (FFT) of a different nanowire showing a nanocrystal in a twinned epitaxial relation with Si. **k, l, m** Image, detail and FFT showing endotaxy in a different nanowire in which the process of silicide incorporation is completed. The dark and bright lines around the nanocrystal in panel l are due to diffraction at the crystal interfaces.

Europe PMC Funders Author Manuscripts

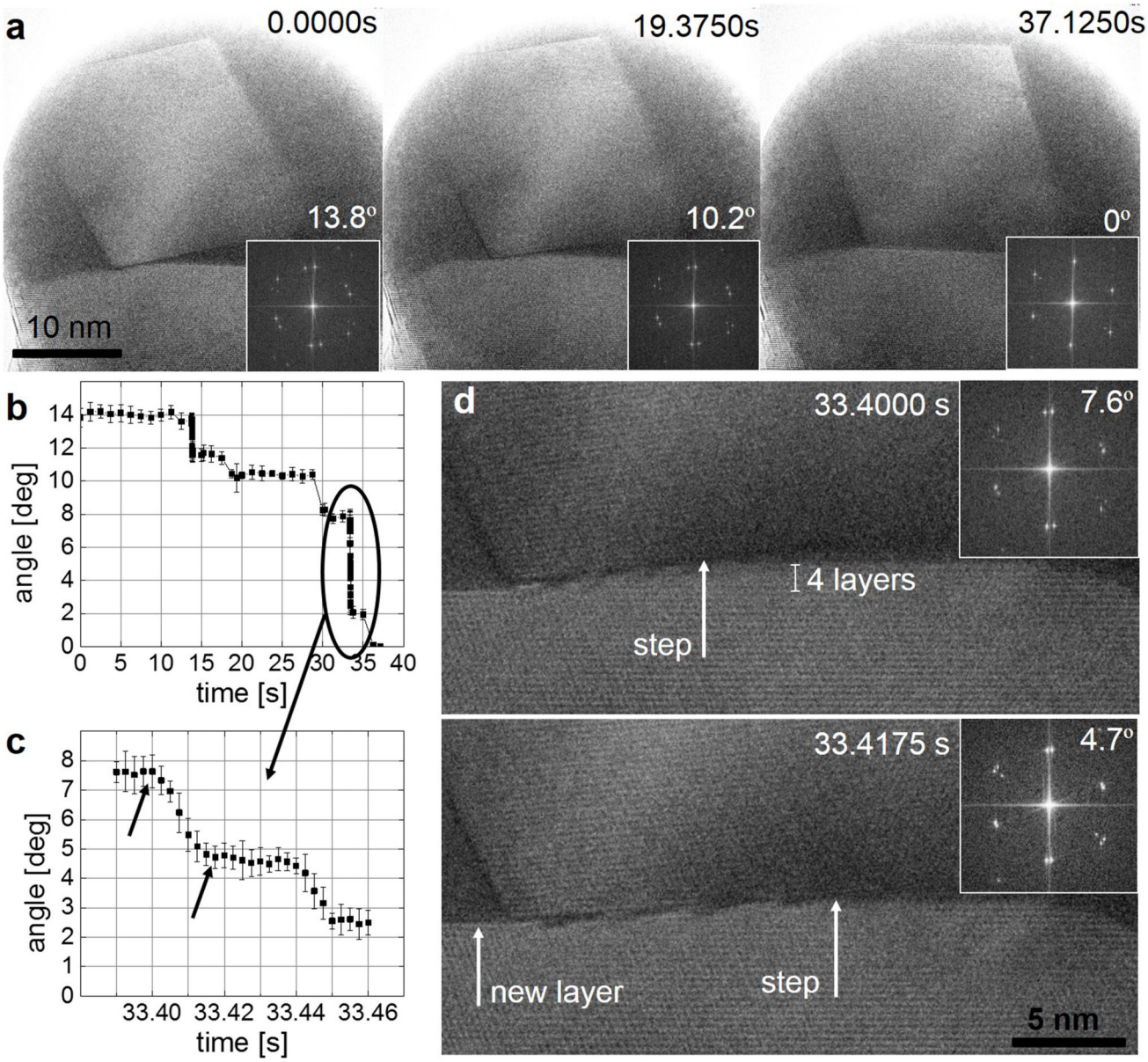

Figure 2.

The docking of a silicide particle with its nanowire. **a** Sequence of atomically resolved, 400 fps TEM images recorded at 400°C. The insets show the FFT of each respective image with the angle between the two crystals indicated. **b** The rotation angle measured from the FFT of the image series in **a** and Movie 2. **c** Detail of **b** showing one larger rotation occurring in two distinct increments; arrows indicate the data corresponding to the images in **d**. **d** Detail of the sequence in **a** showing rearrangement of the Si surface during silicide rotation. The insets show the respective FFTs.

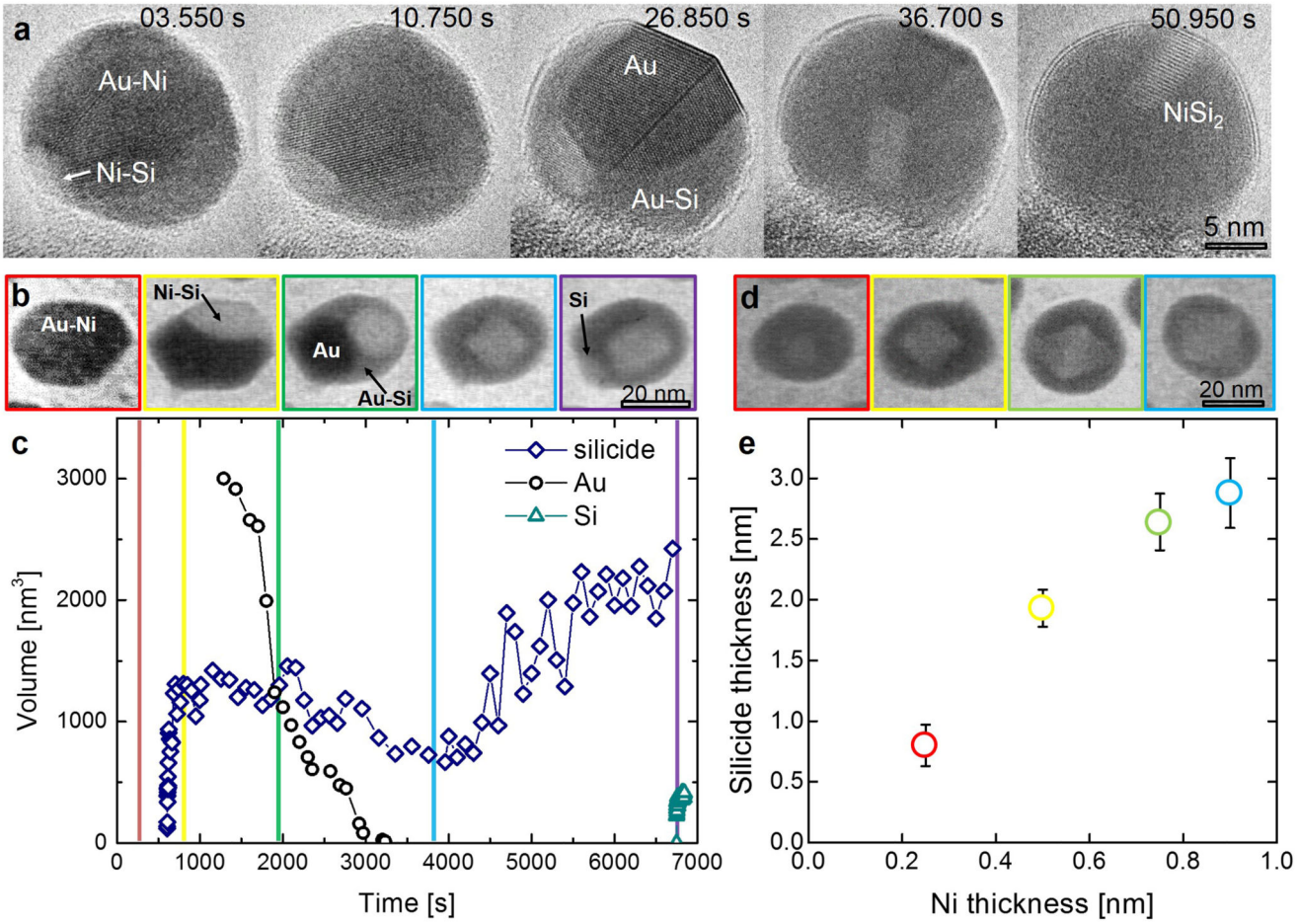

Figure 3.

Ni-silicide nucleation in AuNi nanocrystals deposited on Si nitride membranes. **a** The sequence of phases observed *in situ* in ETEM during exposure of a 7nm radius polycrystalline Au aerosol particle covered with 0.1 nm of Ni to 3.5×10^{-5} Torr of Si_2H_6 at 400°C. The characteristic shape of $NiSi_2$ is first visible in the fourth image. **b** Sequence observed in UHVTEM during exposure of a 15 nm radius polycrystalline Au-Ni crystallite to 3.5×10^{-8} Torr Si_2H_6 at 490°C. 2.5nm Au followed by 0.5 nm Ni were evaporated onto a silicon nitride membrane (see Methods) and agglomerated by annealing in vacuum. **c** Volume versus time of each phase calculated from the projected area and assuming a height equal to the average diameter. Note that the initial silicide volume is overestimated because its shape is far from the assumed ellipsoid; values obtained after disappearance of solid Au are more likely to be accurate. Colored vertical lines identify the time corresponding to images in **c**. **d** Sequence of images of average size silicides formed after the process in **b**, but starting with different amounts of Ni. **e** Colour-coded data of silicide thickness vs. thickness of deposited Ni corresponding to the images in **d**. Silicide thickness is measured by adding the estimated volume of all the silicide nanocrystals recorded in a frame and dividing by its area. Error bar represents the standard deviation calculated by measuring the silicide thickness in 5 different frames.

Europe PMC Funders Author Manuscripts

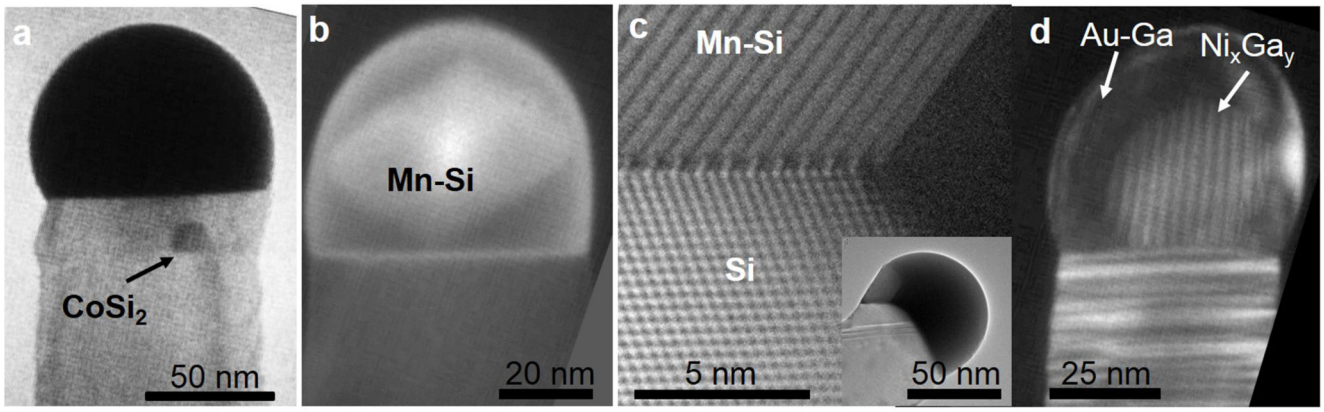

Figure 4.

Nanocrystal formation in different materials. **a** $CoSi_2$ nanocrystal formed after 15 min of exposure to 5×10^{-6} Torr of $Co(C_5H_5)_2$ at 500°C and incorporated into a nanowire after switching to 5×10^{-6} Torr of Si_2H_6 without changing temperature. The Si growth rate after $Co(C_5H_5)_2$ exposure was slower than expected, perhaps suggesting the presence of carbon on the catalyst surface; other metalorganic precursors are known to deposit less carbon at this temperature [42].**b** MnSi nanocrystals formed after Mn evaporation onto the Au-Si catalyst. Similar results are obtained with gas precursor $Mn(C_5H_5)_2$. **c** High resolution image of a Mn-Si nanoparticle in contact with the 111 surface of a nanowire, with the inset showing the whole nanowire. **d** A Ni-Ga nanocrystal formed in a liquid AuGa catalyst on a GaAs nanowire after 20 min exposure to 1×10^{-6} Torr of $Ni(C_5H_5)_2$ at 500°C; image recorded after cooling.

Europe PMC Funders Author Manuscripts